



Article

ZnSe \subset MoSe₂/rGO Petal-like Assembly as Fast and Stable Sodium Ion Storage Anodes

Haoliang Xie ^{1,2}, Shunxing Chen ^{1,2}, Lianghao Yu ³ , Guang Chen ^{1,2,*}, Huile Jin ^{1,2,*}, Jun Li ^{1,2}, Shun Wang ^{1,2} and Jichang Wang ^{4,*}

¹ Key Lab of Advanced Energy Storage and Conversion, Zhejiang Province Key Lab of Leather Engineering, College of Chemistry and Materials Engineering, Wenzhou University, Wenzhou 325035, China; a2090674269@163.com (H.X.); sxchen2023@163.com (S.C.); junli@wzu.edu.cn (J.L.); shunwang@wzu.edu.cn (S.W.)

² Zhejiang Engineering Research Center for Electrochemical Energy Materials and Devices, Institute of New Materials and Industrial Technologies, Wenzhou University, Wenzhou 325035, China

³ Key Laboratory of Spin Electron and Nanomaterials of Anhui Higher Education Institutes, Suzhou University, Suzhou 234000, China; lhyu@ahsuzu.edu.cn

⁴ Department of Chemistry and Biochemistry, University of Windsor, Windsor, ON N9B 3P4, Canada

* Correspondence: chenguang@wzu.edu.cn (G.C.); huilejin@wzu.edu.cn (H.J.); jwang@uwindsor.ca (J.W.)

Abstract: The development of high energy and power density sodium-ion batteries (SIBs) has attracted increasing interest in the last two decades due to the abundance and cost-effectiveness of sodium resources. Herein, this study developed a self-templating synthetic method to construct MoSe₂ nanosheets which were intercalated by ZnSe nanoparticles and were anchored on the in situ reduced graphene oxide layers. The thus-fabricated composites exhibited excellent Coulombic efficiency, a remarkable rate capability and an exceptionally long cycle life when being utilized as the anode in SIBs. Specifically, a reversible capacity of 265 mAh g⁻¹ was achieved at 20 A g⁻¹, which could be maintained for 6400 cycles. At an ultra-high rate of 30.0 A g⁻¹, the anode retained a capacity of 235 mAh g⁻¹ after 9500 cycles. Such a strong performance was attributed to its unique porous structure and synergistic interactions of multi-components. The underlying sodium storage mechanism was further investigated through various techniques such as in situ X-ray diffraction spectroscopy, the galvanostatic intermittent titration method, etc. Overall, this study illustrates the great potential of clad-structured multicomponent hybrids in developing high-performance SIBs.



Citation: Xie, H.; Chen, S.; Yu, L.; Chen, G.; Jin, H.; Li, J.; Wang, S.; Wang, J. ZnSe \subset MoSe₂/rGO Petal-like Assembly as Fast and Stable Sodium Ion Storage Anodes. *Batteries* **2024**, *10*, 447. <https://doi.org/10.3390/batteries10120447>

Academic Editor: Jae-won Lee

Received: 29 October 2024

Revised: 4 December 2024

Accepted: 12 December 2024

Published: 17 December 2024



Copyright: © 2024 by the authors. Licensee MDPI, Basel, Switzerland. This article is an open access article distributed under the terms and conditions of the Creative Commons Attribution (CC BY) license (<https://creativecommons.org/licenses/by/4.0/>).

1. Introduction

The steadily increasing demand for portable electronic devices and electric automobiles has created a great need for batteries with high energy and power densities [1], which are currently dominated by lithium-based batteries. Because of the abundance and affordability of sodium, as well as its similar chemical properties to lithium [2], sodium-ion batteries (SIBs) are being intensively explored as an appealing alternative to lithium-ion batteries. Specifically, Na/Na⁺ has a reduction potential of -2.71 V (vs. SHE), which is similar to that of Li/Li⁺. Such a redox potential will lead to a high energy density and make SIBs increasingly appealing for use in next-generation rechargeable batteries [3]. Unfortunately, sodium ions (Na⁺) have a radius of 1.02 \AA , which is significantly larger than that of lithium ions (Li⁺: 0.76 \AA), which may result in irreversible structural changes in the electrodes and slow down the charging/discharging redox kinetics. This adversely affects their cycling durability and their performance at low multiplication rates. Therefore, developing suitable anode materials is crucial for constructing high-performance SIBs [4]. On this front, researchers have explored various options, such as metal sulfides/selenides/phosphides and intermetallic compounds [4].

Among these newly developed anode materials, two-dimensional metal selenides have demonstrated great potential because of their high energy density and low diffusion barriers in conversion reactions. Among them, molybdenum diselenide (MoSe_2) is being extensively studied as a promising reagent for high-performance SIBs [5]. However, MoSe_2 has a high surface energy and weak van der Waals forces between its layers, which often lead to the collapse of its few-layer structures during charging/discharging. Overall, such a chemical property results in a limited capacity and performance [6]. To overcome these limitations, a commonly used approach is to create nanocomposites by incorporating various carbon materials with MoSe_2 [7]. Additionally, porous nanostructures can be constructed and combined with stable carbon or other materials. The introduction of carbon has several beneficial effects such as enhancing conductivity, mitigating volume changes and preventing the fragmentation and dissolution of intermediates, which ultimately improves cycling stability [8].

Guo et al., for example, proposed a novel approach to preparing bilayer hollow-structured MoSe_2 nanosheets through simultaneous interfacial and electronic structure dual engineering [9]. Similarly, Xu et al. reported the synthesis of hierarchically hybridized materials by incorporating ultrafine ZnSe particles onto or within amorphous nanosized hollow carbon spheres [10]; Huang et al. designed a $\text{Bi}_{2}\text{Se}_{3-x}$ nanoparticle through simple defect chemistry, which significantly mitigated the dissolution and shuttle effects of $\text{Na}-\text{pSex}$ [11]; and Gao and co-workers designed unique heterostructures to generate numerous sodium ion active sites, which endowed $\text{ZnSe}/\text{CoSe}@\text{NC}$ with a relatively strong sodium adsorption capacity [12].

These reported methods demonstrate the improved storage capabilities of sodium, but there are still unresolved issues concerning charge transfer kinetics. On this front, graphene has shown more promising properties among the various carbon materials studied due to its highly conductive network for charge transportation and impressive mechanical strength [13]. Therefore, establishing a strong connection and robust interface between MoSe_2 and graphene presents a promising strategy to achieve efficient redox reaction kinetics and maintain a stable electrode structure [14]. Inspired by these factors, this study developed a procedure to fabricate a unique coating structure [15].

The synthetic approach developed in this study offers several advantages. Firstly, the direct use of GO minimizes aggregation, leading to a more efficient anchoring of MoSe_2 on graphene films [16]. Overall, incorporating an rGO thin film as a conductive substrate enhances the conductivity of the MoSe_2 layer and ZnSe nanospheres and creates suitable porous structures [17], facilitating more efficient electron transmission and ion diffusion [18]. Secondly, the utilization of rGO as a coating for these materials effectively suppresses the expansion and agglomeration exhibited by MoSe_2 , thus prolonging the battery's cycle life [19]. Additionally, the intercalation and coating of ZnSe nanoparticles also effectively suppress the volume expansion and structural transformation of MoSe_2 , thereby leading to the enhanced stability of the composite material during charge/discharge cycles [20]. The porous structure and increased interlayer spacing of MoSe_2 sheets and ZnSe nanospheres provide favorable conditions for sodium ion storage [21].

The larger interlayer distance of MoSe_2 (≈ 0.64 nm) also improves the cycling stability of the electrode and reduces structural damage to the material [22]. Meanwhile, the inhibitory effect of ZnSe particles is significant in mitigating undesirable reactions and processes within the battery system [23], which also lowers the risk of material degradation, and improves the overall stability and reliability of the sodium-ion battery [24]. As a result, this newly fabricated materials, which possess a distinctive sandwich multi-component hierarchical structure, demonstrates an exceptional rate performance and cycling stability as the anode material in SIBs [25]. Specifically, at a high charge/discharge current of 30 A g^{-1} it achieved a remarkable reversible capacity of 238 mAh g^{-1} after undergoing 9500 cycles.

2. Materials and Methods

Materials: Monolayer graphene oxide dispersed in water was purchased from Hangzhou Gaoxi Technology Co., Ltd. (Hangzhou, China). Ammonium heptamolybdate tetrahydrate ($(\text{NH}_4)_6\text{Mo}_7\text{O}_{24} \cdot 4\text{H}_2\text{O}$), zinc nitrate hexahydrate, ethanol, methanol, 2-methylimidazole and selenium (Se) were purchased from Shanghai Aladdin Industrial Co. (Shanghai, China). All chemicals were analytical grade ($\geq 99.0\%$) and were used without further purification.

Synthesis procedure: Firstly, 1.4 g of $(\text{NH}_4)_6\text{Mo}_7\text{O}_{24} \cdot 4\text{H}_2\text{O}$ was dissolved in 40 mL ($2.4 \text{ mol} \cdot \text{L}^{-1}$, 6.4 mL) of nitric acid with stirring. The mixture was stirred for 20 min before being transferred to a 50 mL Teflon-lined stainless steel autoclave. After keeping the mixture at 180°C for 12 h, the steel reactor was naturally cooled to room temperature. Solid products were collected by centrifugation, washed multiple times with deionized water and ethanol and then dried at 60°C overnight, resulting in the production of MoO_3 . TEM images of this product are shown in Supporting Information (Figure S7a,b).

In the next stage, a solution was prepared by adding 1.0 g of graphene oxides, 0.1 g of synthesized molybdenum oxide powder and 0.36 g of zinc nitrate hexahydrate to 40 mL of methanol, followed by sonication for 30 min. After sonication, a solution consisting of 1.64 g of 2-methylimidazole and 40 mL of methanol was added to the solution under vigorous stirring. After being subjected to 6 h of stirring, the above mixture was allowed to stand for another 48 h. The solid product, denoted as $\text{MoO}_3\text{-Zn/rGO}$, was collected by centrifugation and washed with deionized water and ethanol to remove residues and impurities.

Finally, the $\text{MoO}_3\text{-Zn/rGO}$ composite material obtained above was grounded and blended with selenium powder in a ratio of 1:4. The well-dispersed solids above were thermal treated at 700°C for 3 h using a tube furnace at 0–0.1 MP pressure and a flow rate of 10–15 sccm of 5% hydrogen and 95% argon flow. The furnace temperature increased at a rate of 5°C min^{-1} to reach the pre-determined temperature. This process yielded $\text{ZnSe}\subset\text{MoSe}_2/\text{rGO}$ composite materials. The ICP technique was deployed to determine the masses of Mo and Zn in the sample, which subsequently allowed us to calculate the mass of MoSe_2 and ZnSe in the composites (Figure S8).

Additionally, this study also employed the same method to synthesize $\text{ZnSe}\subset\text{MoSe}_2$ composite materials (i.e., without carbon). Specifically, the reaction followed the same steps, but without the addition of graphene oxides. The material generated in this study was determined to be $\text{ZnSe}\subset\text{MoSe}_2$.

Characterization: X-ray photoelectron spectroscopy (XPS) measurements were performed using a Kratos Axis Ultra DLD spectrometer with Mono AlKa radiation (120 W, 8 mA, 15 kV) (Thermo Fisher Scientific, Waltham, MA, USA). Scanning electron microscopy (SEM) images were obtained with a Novanos EM200 system, operating at an acceleration voltage of 10 kV. X-ray diffraction (XRD) patterns were recorded using a Bruker D8 Advance diffractometer (Bruker, Valcz Bach, Berlin, Germany), with CuKa radiation ($\lambda = 0.15406 \text{ nm}$), and data were collected over a 2θ range of 5° to 80° with a step size of 0.05° . Transmission electron microscopy (TEM) and energy dispersive X-ray spectroscopy (EDS) were conducted on a JEOL-2100 instrument (JEOL, Tokyo, Japan). Raman spectroscopy was carried out with an InVia spectrophotometer (Renishaw, Pliezhausen, Germany) using a 514 nm laser. Nitrogen adsorption and desorption isotherms were measured at liquid nitrogen temperature using a Micrometrics ASAP 2020 (Mai ke mo Rui ti ke (Shanghai) instrument Co., Ltd., Shanghai, China) surface area and pore size analyzer. The nitrogen content of the samples was determined with a carbon–hydrogen–nitrogen (CHN) analyzer (Perkin-Elmer CHN-2400, Perkin Elmer, Waltham, MA, USA).

Preparation of $\text{ZnSe}\subset\text{MoSe}_2/\text{rGO}$ composite electrodes: According to the mass ratio of the $\text{ZnSe}\subset\text{MoSe}_2/\text{rGO}$ composite material–acetylene black–PVDF, which was 7:2:1, 70.0 mg of $\text{ZnSe}\subset\text{MoSe}_2/\text{rGO}$ composite, 20.0 mg of acetylene black, 10.0 mg of PVDF and 1.0 mL of anhydrous N-methylpyridinone were mixed in a tank to form homogeneously dispersed slurry. Uniform electrodes with a thickness of $20 \mu\text{m}$ were then fabricated by coating the above slurry on copper foil, using a lab battery film coater coating machine. The pre-coated electrode sheet was placed into a vacuum drying oven and dried at 80°C for 9 h.

We then cut out circular pieces with a diameter of 12 mm from the dried electrode sheet and weighed the mass of each circular piece. Based on the ICP measurements, the mass of ZnSe_xMoSe₂ was found to be about 62.5% of the as-synthesized composites and the rest were carbon materials that consisted of rGO and N-doped carbon. The capacity reported in this study is based on the mass of the ZnSe_xMoSe₂ active materials, which is calculated by taking the weight of the coated copper circle and subtracting the mass of copper and then multiplying the result by 70% (mass ratio of ZnSe_xMoSe₂/rGO composites in slurry) and then multiplying it by 62.5% (mass ratio of ZnSe_xMoSe₂ in the composites).

Assembly of batteries: The half-cell assembly was carried out in a glove box filled with argon gas ($\text{H}_2\text{O} < 0.05 \text{ ppm}$, $\text{O}_2 < 0.05 \text{ ppm}$). The assembly of the cleaned coin battery consisted of C2025 shells, a sodium sheet (15.6 mm in diameter and 0.44 mm in thickness), a glass fiber diaphragm disk (GF/A, 16 mm in diameter) as a separator, a ZnSe_xMoSe₂/rGO compositized electrode, a stainless steel gasket, a stainless steel shunt and $1.0 \text{ mol}\cdot\text{L}^{-1}$ NaPF6-DIGLYME as the electrolyte, which were compressed together in the above order with a tablet press. When assembling a full cell, it was necessary to use a $\text{Na}_3\text{V}_2(\text{PO}_4)_3$ wafer (12 mm in diameter and 0.44 mm in thickness) as the cathode and replace the sodium sheet with a ZnSe_xMoSe₂/rGO composite electrode as the anode. The electrolyte in the full cell was changed to an ether-based electrolyte. The rest of the operation was the same as described above.

3. Results and Discussion

A schematic of the synthesis procedure of ZnSe_xMoSe₂/rGO hybrids is shown in Figure 1a. In this method, GO flakes, ammonium heptamolybdate tetrahydrate ($(\text{NH}_4)_6\text{Mo}_7\text{O}_{24}\cdot 4\text{H}_2\text{O}$), Se powder and $\text{Zn}(\text{NO}_3)_2\cdot 6(\text{H}_2\text{O})$ were used as the starting reagents, which were the sources of rGO, molybdenum, Se and Zn, respectively. The hydrothermal reaction was applied to promote the growth of MoSe₂ nanosheets on graphene oxide flakes. Unlike MoSe₂ which formed two-dimensional nanosheets, ZnSe nanoparticles were generated on these MoSe₂ flakes (as seen in Figure 1d in which the blue circles are ZnSe). Figure 1f shows that a small lattice of ZnSe (200) is present on the large plane of the MoSe₂ (100) and (102) flakes.

The microstructures of the above-synthesized ZnSe_xMoSe₂/rGO composites were investigated using FESEM and TEM. The measurements revealed that ZnSe_xMoSe₂ was synthesized even in the absence of the GO substrate, in which the reaction resulted in irregular shaped products, as depicted in Figure S2a,b (Supporting Information). Figure 1b,c showcase panoramic FESEM images of ZnSe_xMoSe₂/rGO, which highlight the distinctive petal-like morphology and impressive yield of the composites. The dispersion of nanosheets and particles on the 2D graphene film enables the formation of a typical coating structure with diverse pore sizes, offering various advantages including enhanced electrolyte penetration and ion transportation [26]. The conductivity of this hybrid material was further enhanced through the high-temperature treatment of graphene [27]. TEM measurements (see Figure S2a,b) support the findings observed in the FESEM images, and Figure S2 clearly show the intimate contact between the rGO substrate and MoSe₂ flakes that are indicated by blue circles in Figure 1d. Additionally, the TEM also reveals the structural characteristics of this hybrid material. Notably, in addition to the nanospheres present on the surface, there are numerous embedded ZnSe NPs within the flake of MoSe₂.

The HRTEM image in Figure 1e primarily exhibits lattice spacing belonging to MoSe₂, with approximate values of 2.61, 2.38 and 2.84 Å. These numbers match the (100), (102) and (103) lattice planes of MoSe₂. Meanwhile, Figure 1f displays lattice fringes ($d = 2.03 \text{ \AA}$) originating from the lattice planes of the (200) ZnSe nanoparticle. Its formation may be attributed to the evaporation of zinc from polyhedral during the high-temperature calcification and subsequent adsorption on the graphene nanosheets. Moreover, the MoSe₂ layer exhibits an enlarged interlayer spacing (6.78 Å). This increased space favors the insertion/extraction of Na^+ ions [28].

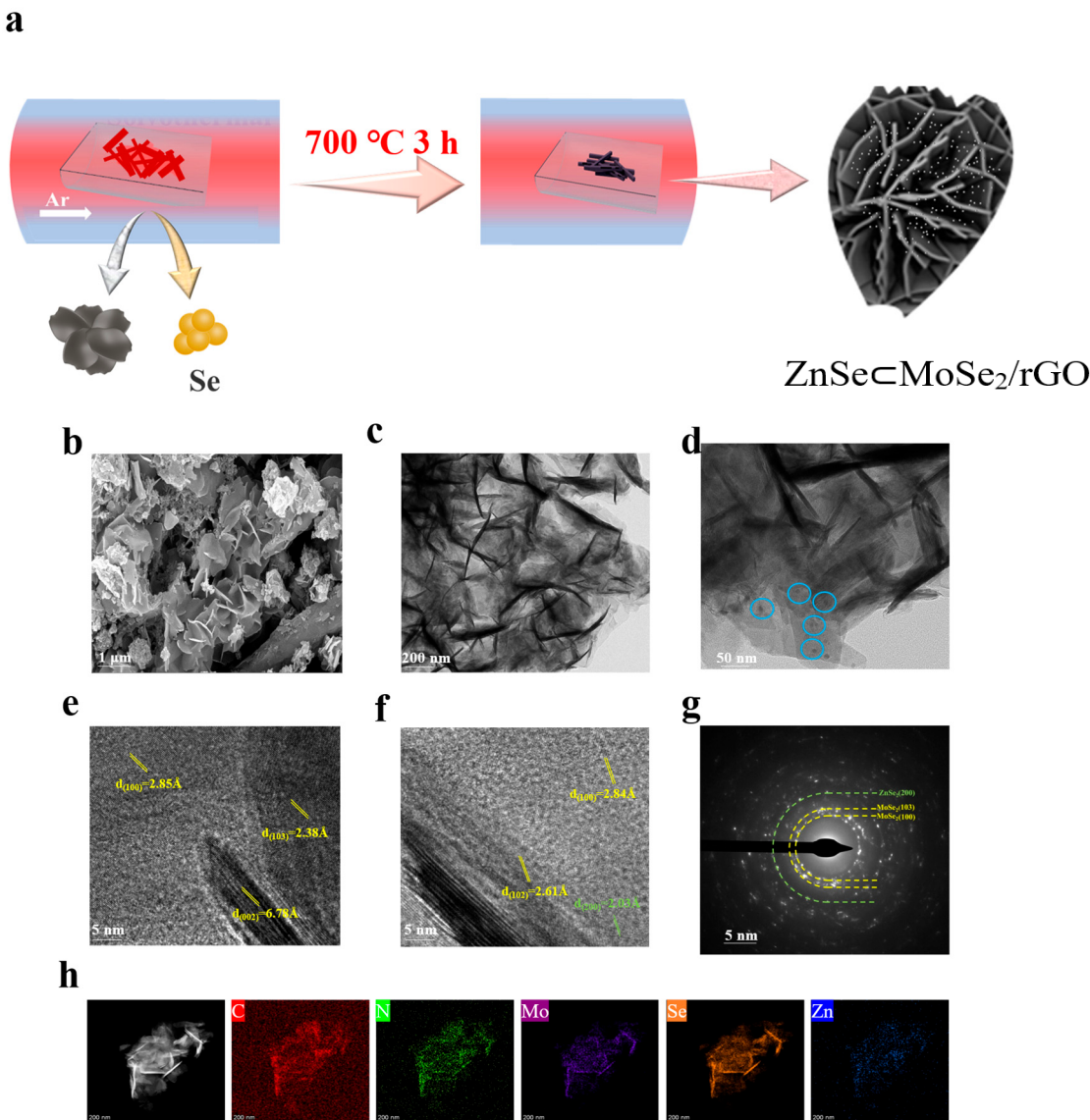


Figure 1. Morphology and structure of ZnSe \subset MoSe₂/rGO hybrids. (a,b) FESEM images; (c–f) transmission electron microscopy images; (g) SAED maps of the corresponding ZnSe \subset MoSe₂/rGO; (h) and SAED maps of ZnSe \subset MoSe₂/rGO hybrids. The STEM-EDX elemental maps clearly show how C (red), N (green), Zn (blue), Se (yellow) and Mo (purple) are distributed.

The SAED spectrum in Figure 1g confirms that the above hybrid composites contain both MoSe₂ and ZnSe. It displays a Debye–Scherrer ring diagram representing the crystal planes (103) and (100) of MoSe₂ and the (200) crystal plane of ZnSe. Additionally, the STEM image in Figure 2h, taken in HAADF mode, offers direct evidence about the structural characteristics of ZnSe \subset MoSe₂/rGO. It clearly shows that MoSe₂ sheets are uniformly anchored on the graphene sheet, while ZnSe particles are randomly deposited on these MoSe₂ flakes. To further discern the structural features, elemental mapping with EDS was also conducted (see Figure 1h), which showed the uniform presence of Zn, Mo and Se on these graphene flakes.

The structure and chemical compositions of the above products were also characterized with XRD. Figure 2a depicts the XRD pattern of ZnSe \subset MoSe₂/rGO, showing distinct peaks at 31.5°, 37.9° and 55.9°, which can be attributed to the (100), (103) and (110) planes of hexagonal MoSe₂ (PDF 29–0914), respectively. Notably, no impurity-induced peaks are observed. Additionally, the peaks at 27.3°, 45.4° and 53.6° can be attributed to the (111), (220) and (311) indices of cubic ZnSe (PDF 37–1463). Our investigation indicates that the

characteristic peak of the (002) phase gradually weakens as a result of the increasing rGO content. It suggests an effective reduction in the MoSe₂ layer's stacking due to the graphene. Furthermore, no other diffraction peaks were observed, which confirmed the high purity and crystallinity of these products.

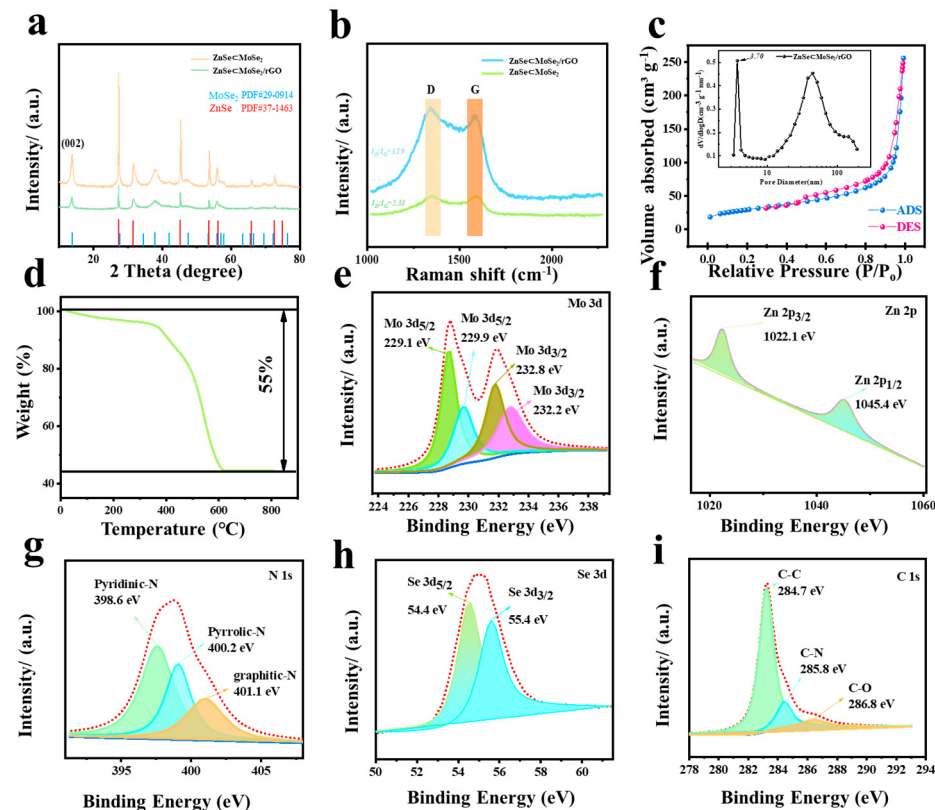


Figure 2. Characterization of ZnSeMoSe₂/rGO hybrids. (a) XRD pattern; (b) Raman spectrum; (c) N₂ adsorption isotherm and corresponding pore size distribution; (d) TGA curve; and (e–i) high-resolution spectra of Mo 3d; Zn 2p; Se 3d; N 1s; and C 1s.

A Raman spectroscopy analysis of ZnSeMoSe₂/rGO confirmed the presence of MoSe₂, ZnSe and carbon (Figure 2b), in which the spectrum exhibited peaks at 1351 and 1586 cm⁻¹, corresponding to the D band and G band of rGO, respectively. The high-intensity ratio of I_D/I_G indicates the presence of abundant defects in carbon, which can be attributed to the attachment of MoSe₂ and ZnSe, as well as N doping [29]. The higher inner diameter I_D/I_G ratio observed in the ZnSeMoSe₂/rGO composites (3.39) compared to the ZnSeMoSe₂ composites (2.33) suggests a greater presence of defects in the former. The reduced agglomeration of MoSe₂ flakes and ZnSe nanoparticles within the composites are expected to provide more electrochemical reaction sites, thereby promoting a pseudocapacitive behavior on the surface [30].

Figure 2c depicts the N₂ adsorption/desorption isotherms and pore size distribution of ZnSeMoSe₂/rGO composites. The BET specific surface area, calculated using the BET isotherm, is significantly higher ($99.64 \text{ m}^2 \text{ g}^{-1}$) than that of the material synthesized without graphene oxides (i.e., only $3.92 \text{ m}^2 \text{ g}^{-1}$, see Figure S3 in the Supporting Information). The wide peaks at 10–100 nm in Figure 2c are because the addition of graphene enables the hybrids to form various forms of larger pores, which shortens the diffusion distance of Na⁺. Such a porous structure would also enhance the contact between the composites and electrolytes. This larger specific surface area provides more sites for electrochemical reactions. Additionally, a large number of pores ranging from 4 to 10 nm buffers the volume expansion of the ZnSeMoSe₂/rGO composites during sodium storage.

From the results of ICP-AES measurements, Mo and Zn were calculated to have a molar ratio of 1:0.92. To determine the carbon content of the composites, we combined the results of thermogravimetric analyses (TGAs) and ICP. During the TGAs (See Figure 2d), the mass of the sample gradually decreased because of SeO_2 sublimation and carbon oxidation. Combining the overall weight loss data with the known Mo/Zn molar ratio, we calculated that the composites contained about 28.6% carbon. Such an amount of carbon seems to be enough to support MoSe_2 and ZnSe and enhance their conductivity.

To analyze the chemical compositions and surface electronic states, XPS was also utilized to measure the above $\text{ZnSe}\subset\text{MoSe}_2/\text{rGO}$ composites. The full scan range revealed the presence of Mo, Zn, Se, N and C in the material (Figure S4a). Such an observation is consistent with the STEM-EDX mapping results. Furthermore, the high-resolution Mo 3d spectrum (Figure 2e) exhibited two pairs of peaks at 229.1 and 229.9 eV and 232.8 and 232.2 eV, corresponding to Mo $3d_{5/2}$, Mo $3d_{3/2}$ and their satellite peaks, indicating the presence of Mo^{4+} [31]. The high-resolution Zn 2p spectrum (Figure 2f) showed two peaks at 1022.1 eV for Zn $2p_{3/2}$ and 1045.4 eV for Zn $2p_{1/2}$, confirming the presence of Zn^{2+} . Additionally, the high-resolution Se 3d spectrum (Figure 2g) displayed two peaks at 54.4 and 55.4 eV, which could be attributed to Se $3d_{5/2}$ and Se $3d_{3/2}$ in MoSe_2 , indicating the existence of Se^{2-} [32].

The N 1s spectrum (Figure 2h) exhibited three peaks at 398.6, 400.2 and 401.4 eV. These peaks are attributed to pyridine-N, pyrrolic acid-N and graphite-N. Similarly, the C 1s spectrum (Figure 2i) displayed three peaks at 284.7 eV (C-C), 285.8 eV (C-N) and 286.8 eV (C-O). The presence of C-N bonds and graphite N further confirms that N atoms have been successfully doped into the carbon framework.

The electrochemical activity of the $\text{ZnSe}\subset\text{MoSe}_2/\text{rGO}$ composites as the SIB anode was evaluated using half-cells. These tests were conducted between 0.01 and 3.0 V (Na^+/Na). Figure 3a shows the first three cyclic voltammetry (CV) curves. In the initial cathodic scan, scanned at the rate of 0.1 mV s^{-1} , two peaks were observed, where the first cathodic peak at 0.736 V corresponded to the insertion of Na ions into the interlayer of MoSe_2 , resulting in the formation of Na_xMoSe_2 . The second peak at 0.373 V indicates further Na_xMoSe_2 reduction to form metallic molybdenum and Na_2Se as well as the formation of a solid electrolyte layer [33]. Moreover, during the charging (anode) process, the peaks at 0.955 V and 1.686 V likely arose from the oxidation of Mo, forming MoSe_2 . Additionally, a small peak is observed at 1.505 V, which likely originated from the dealloying reaction of NaZn_{13} alloy. In the following cycles, these CV curves exhibit remarkable overlap, suggesting the excellent stability and reversibility of $\text{ZnSe}\subset\text{MoSe}_2/\text{rGO}$ as anode material.

Figure 3b shows the $\text{ZnSe}\subset\text{MoSe}_2/\text{rGO}$ electrode's galvanostatic discharge/charge curve at 0.1 A g^{-1} . The initial discharge capacity is observed to be 528.7 mAh g^{-1} , whereas the charge capacity is 446.8 mAh g^{-1} . Such a result suggests that its initial Coulombic efficiency (ICE) is 84.5%. In contrast, the ICE of the composite material without rGO is 72.7% (Figure S4b). The initial irreversible capacitance loss is attributed to the formation of the solid electrolyte interphase (SEI) layer. The comparative rate performance of the two electrodes at different currents is depicted in Figure 3c. The reversible capacities of the $\text{ZnSe}\subset\text{MoSe}_2/\text{rGO}$ electrode at $2, 5, 10, 15, 20$ and 30 A g^{-1} are $288.8, 279.9, 275.5, 266.6, 250.5$ and 244.4 mAh g^{-1} , respectively. Notably, the discharge capacity of $\text{ZnSe}\subset\text{MoSe}_2$ electrode is significantly lower when compared to that of the $\text{ZnSe}\subset\text{MoSe}_2/\text{rGO}$ electrode at the same current.

Significantly, the capacity of the $\text{ZnSe}\subset\text{MoSe}_2/\text{rGO}$ electrode was almost fully restored when the current density was reduced back to 0.1 A g^{-1} , indicating an excellent electrochemical stability. Furthermore, the rate performance of $\text{ZnSe}\subset\text{MoSe}_2/\text{rGO}$ hybrids surpassed previous reports on SIBs anode materials, especially at high current densities (see Figure 3d). Finally, the cycling stability of both $\text{ZnSe}\subset\text{MoSe}_2/\text{rGO}$ and $\text{ZnSe}\subset\text{MoSe}_2$ electrodes was evaluated at 20 A g^{-1} . The data in Figure 3e illustrate the exceptional cycling stability of the $\text{ZnSe}\subset\text{MoSe}_2/\text{rGO}$ electrode, achieving approximately 100% Coulombic efficiency. After undergoing 6400 cycles at 20 A g^{-1} , the electrode maintained a highly

reversible capacity of 265 mAh g^{-1} , which is significantly higher than 116 mAh g^{-1} of the $\text{ZnSe}\subset\text{MoSe}_2$ electrode. Furthermore, the excellent cycling performance of both composites is further demonstrated in Figure 3f. After undergoing 9500 cycles at 30 A g^{-1} , the capacity of the $\text{ZnSe}\subset\text{MoSe}_2/\text{rGO}$ electrode remains at 238 mAh g^{-1} , whereas the $\text{ZnSe}\subset\text{MoSe}_2$ electrode remains 126 mAh g^{-1} . This leads to an impressive capacity retention of up to 77%.

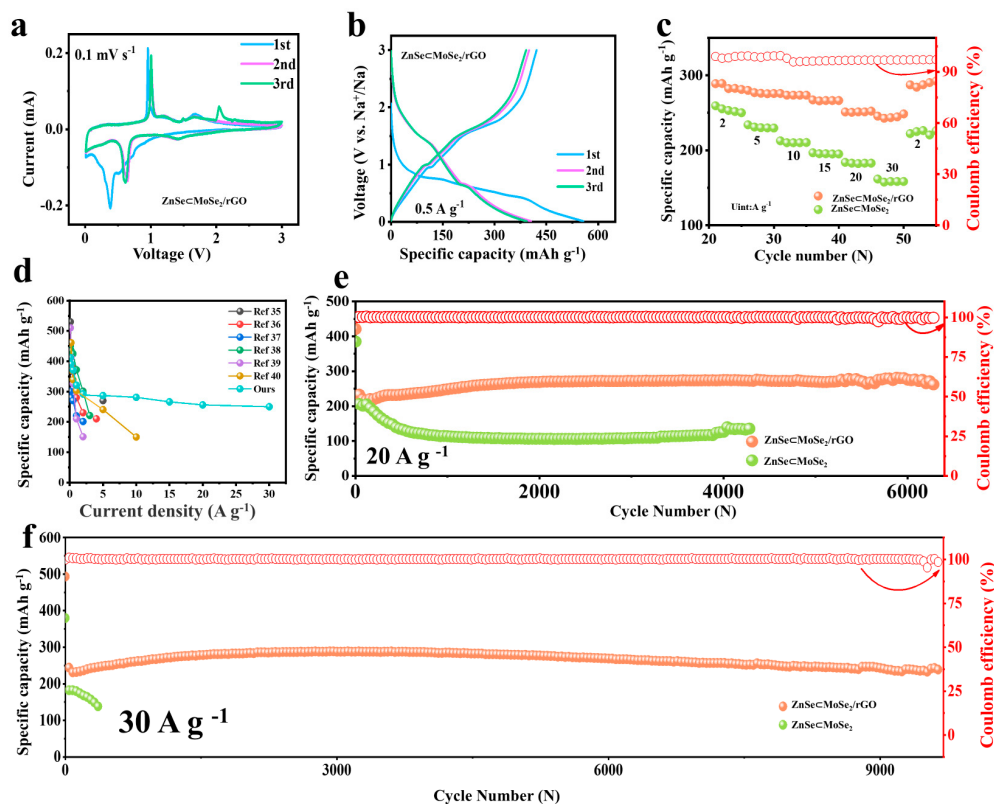


Figure 3. Electrochemical characterization: (a) CV curve and (b) GCD curve. (c) Rate performance of $\text{ZnSe}\subset\text{MoSe}_2/\text{rGO}$ and $\text{ZnSe}\subset\text{MoSe}_2$ electrodes. (d) Performance comparison of our work with other materials. (e,f) Cycling performance of $\text{ZnSe}\subset\text{MoSe}_2/\text{rGO}$ and $\text{ZnSe}\subset\text{MoSe}_2$ electrodes at 20 A g^{-1} and 30 A g^{-1} , respectively.

The above results unequivocally demonstrate that $\text{ZnSe}\subset\text{MoSe}_2/\text{rGO}$ outperforms $\text{ZnSe}/\text{MoSe}_2$ in terms of its cycling stability and rate capabilities, underscoring the remarkable electrochemical properties bestowed by graphene. The constructive contribution of graphene in the above composites may be understood from the following aspects: Firstly, its large surface area provides additional connection points for discharge products. Secondly, graphene effectively prevents the agglomeration of MoSe_2 via offering abundant attachment points for MoSe_2 . The graphene substrate also suppresses the volume fluctuation of MoSe_2 associated with discharging/charging. The unique structural characteristics of $\text{ZnSe}\subset\text{MoSe}_2/\text{rGO}$ hybrids leads to the above remarkable cycle performance.

To further characterize the electrochemical activity of $\text{ZnSe}\subset\text{MoSe}_2/\text{rGO}$ hybrids, this study also conducted kinetic analysis using CV curves and EIS. Figures 4a and S5a display the CV curves of $\text{ZnSe}\subset\text{MoSe}_2/\text{rGO}$ and $\text{ZnSe}\subset\text{MoSe}_2$ electrodes at a scan rate ranging from 0.2 to 1.0 mV s^{-1} . With the increase in the scan rate these redox peaks gradually broadened, indicating prominent pseudo capacitance and low polarization characteristics [34]. By examining the relationship between peak current and scan rate (i.e., ii vs. v) we obtain the following:

$$i = av^b \quad (1)$$

$$\log(i) = \log(a) + b \times \log(v) \quad (2)$$

where a is a constant and the value of b can be obtained from the slope of the $\log(i)$ vs. $\log(v)$ plot. A value of $b = 0.5$ indicates a diffusion-controlled Faraday process, while a value of $b = 1.0$ indicates capacitively controlled behavior. The b values for the cathode peak and the anode peak in Figure 4b are 0.967 and 0.818, respectively, suggesting that electrochemical processes at the $\text{ZnSe}\subset\text{MoSe}_2/\text{rGO}$ electrode are predominantly governed by surface-induced capacitance.

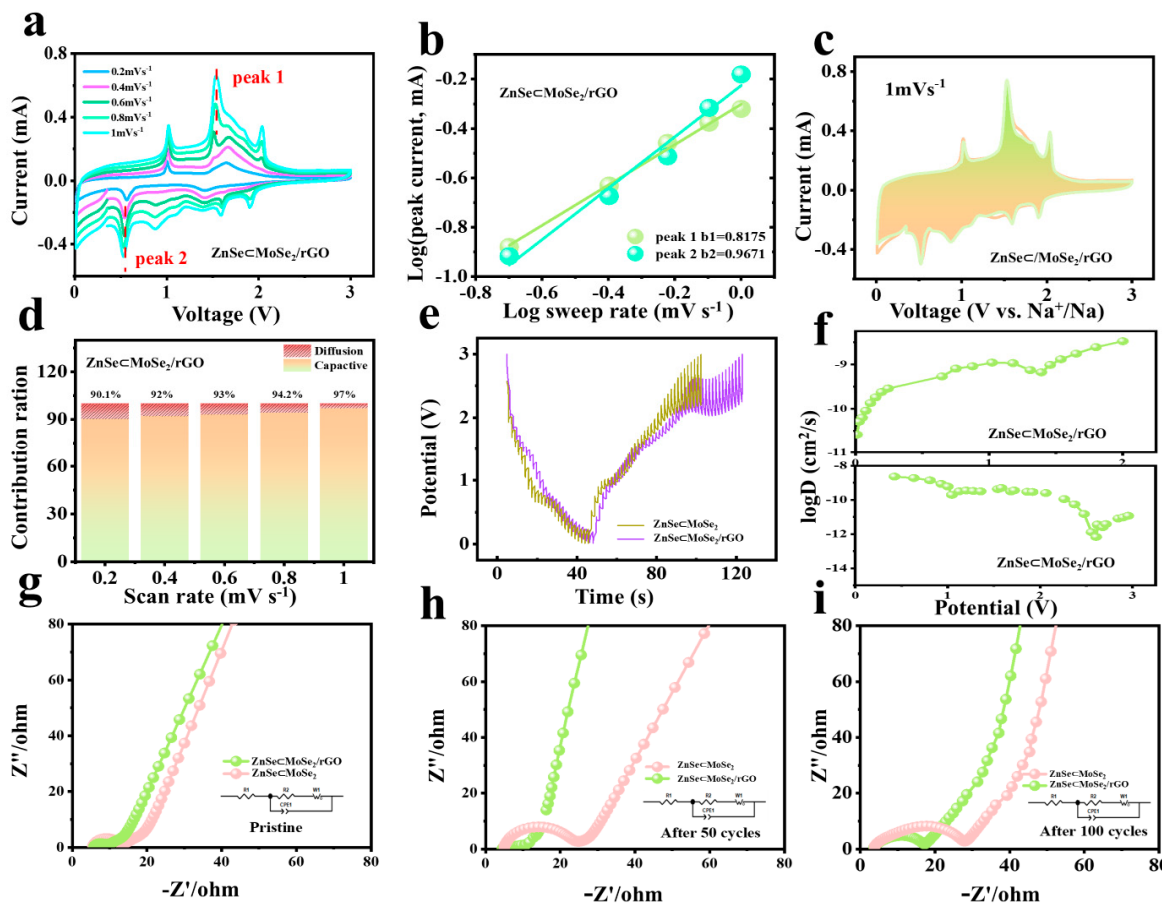


Figure 4. (a) CV curves of $\text{ZnSe}\subset\text{MoSe}_2/\text{rGO}$ at different scan rates; (b) the relationship between peak current and scan rate; (c) the capacitance contribution of $\text{ZnSe}\subset\text{MoSe}_2/\text{rGO}$ at a scan rate of 1.0 mV^{-1} (color filled area); (d) the contribution ratio of capacitance contribution at different scan rates; (e) the GITT voltage diagram; (f) diagram of the change in the sodium ion diffusion coefficient; (g) the EIS of $\text{ZnSe}\subset\text{MoSe}_2/\text{rGO}$ and $\text{ZnSe}\subset\text{MoSe}_2$ electrodes; (h) EIS after 50 cycles; and (i) EIS after 100 cycles.

Capacitive behavior is also observed with the $\text{ZnSe}\subset\text{MoSe}_2$ electrode, as shown in Figure S5b. The capacity contribution is determined with the equation $i(V) = k_1v + k_2v^{1/2}$, where k_1v and $k_2v^{1/2}$ correspond to the capacitance effect and the diffusion control effect. Figures 4c and S5c reveal that the capacitance contributions of $\text{ZnSe}\subset\text{MoSe}_2/\text{rGO}$ and $\text{ZnSe}\subset\text{MoSe}_2$ at a 1 mVs^{-1} scan rate are 97% and 94.8%, respectively. A higher capacitive contribution indicates faster kinetics of Na^+ storage, resulting in excellent performance at high current densities, particularly in terms of rate capability [35]. Figure 4d demonstrates that the capacitance contribution of the $\text{ZnSe}\subset\text{MoSe}_2/\text{rGO}$ electrode increases to 90.1%, 92%, 93%, 94.2% and 97% at scan rates of $0.2, 0.4, 0.6, 0.8$ and 1.0 mV s^{-1} , respectively. This increase in ratio is more significant compared to the $\text{ZnSe}\subset\text{MoSe}_2$ electrode, as shown in Figure S5d. Furthermore, the advantages of the surface control process become more pronounced with increasing scan rates.

To gain more insights into the electrochemical properties of the above composites, an EIS Nyquist plot and galvanostatic intermittent titration were also conducted for analysis. These measurements provided valuable information about the kinetic differences between these two samples. Specifically, the Na^+ diffusion coefficient (D) of the $\text{ZnSe}\subset\text{MoSe}_2/\text{rGO}$ and $\text{ZnSe}\subset\text{MoSe}_2$ composites could be evaluated with the galvanostatic intermittent titration. Assuming that the transfer of Na^+ follows Fick's second law, the diffusion coefficient can be calculated using the following equation:

$$D_{\text{Na}^+} = \frac{4}{\pi\tau} \left[\left(\frac{m_B V_m}{AM_B} \right) \frac{\Delta E_s}{\Delta E_t} \right]^2 \quad (3)$$

Among these terms, τ represents the constant current titration time; V_m represents the molar volume of the active material; m_B represents the weight of the active material; M_B refers to the molecular weight of the active material; A is the electrode surface area; ΔE_s represents the steady-state voltage change after current interference; ΔE_t represents the voltage change during the constant current titration process.

According to Figures 4e,f and S5e, the $\text{ZnSe}\subset\text{MoSe}_2/\text{rGO}$ electrode was seen to exhibit the highest D_{Na^+} ($2.68 \times 10^{-12} \text{ cm}^2 \text{ s}^{-1}$) during the charging process compared to the D_{Na^+} ($7.68 \times 10^{-14} \text{ cm}^2 \text{ s}^{-1}$) of the $\text{ZnSe}\subset\text{MoSe}_2$ electrodes. The plateau in the $\text{ZnSe}\subset\text{MoSe}_2$ electrode during testing is due to the fact that the process of embedding/de-embedding sodium ions in the material becomes relatively slow or stable in the electrode material. This finding suggests that the $\text{ZnSe}\subset\text{MoSe}_2/\text{rGO}$ electrode has the fastest sodium ion diffusion. The increase in Na^+ diffusion can be ascribed to the smallest charge transfer resistance observed in the EIS of the $\text{hZnSe}\subset\text{MoSe}_2/\text{rGO}$ electrode. As is well documented in the literature, the semicircle in the EIS output is associated with the reaction impedance, while the low-frequency straight line reflects ion diffusion within the electrode.

Both $\text{ZnSe}\subset\text{MoSe}_2/\text{rGO}$ and $\text{ZnSe}\subset\text{MoSe}_2$ electrodes exhibited typical EIS results initially and after 50 cycles, as well as after 100 cycles, as shown in Figure 4g–i. The initial charge reversal resistances (R_{ct}) for the $\text{ZnSe}\subset\text{MoSe}_2/\text{rGO}$ and $\text{ZnSe}\subset\text{MoSe}_2$ electrodes were 4.7 and 8.1 Ω , respectively, which were increased, respectively, to 10.8 and 22.1 Ω after 50 cycles, as per the fitted data. Upon reaching 100 cycles, the resistance values further increased to 16.3 and 26.8 Ω , respectively. The $\text{ZnSe}\subset\text{MoSe}_2/\text{rGO}$ anode consistently exhibited the lower R_{ct} value, both initially and after multiple cycles. These results indicate that the $\text{ZnSe}\subset\text{MoSe}_2/\text{rGO}$ composites possess the highest charge transfer rate among the samples studied, leading to improved rate capability. These attractive electrochemical properties may be ascribed to the unique multi-component coating structure that not only shortens the Na^+ diffusion path but also reduces contact resistance.

To understand the electrochemical reaction processes at the $\text{ZnSe}\subset\text{MoSe}_2/\text{rGO}$ electrode, in situ XRD measurements were conducted during the initial charge and discharge in the potential between 0.01 and 3.0 V. The discharge/charge curve is presented in Figure 5a, while the corresponding XRD pattern is displayed in Figure 5b. Based on these in situ XRD measurements, it can be clearly observed that the intensity of BeO remains steady at 38.4° and 41.6° throughout the discharge and charge processes. The MoSe_2 exhibits two diffraction signals, namely (100) and (110), at 30.2° and 55.8° , respectively. As the sodiation progresses during discharge, the MoSe_2 diffraction peaks of (100) and (110) gradually weaken and eventually vanish. This behavior suggests the incorporation of sodium ions into the host MoSe_2 materials, which results in a poor crystallinity and smaller size. At 36.7° , the intermediate Na_xMoSe_2 is formed. Meanwhile, as seen from point A in Figures 4a and S6a,b, Zn^{2+} begins to be reduced at 1.95 V during the discharge process. The signal peak at 43.03° indicates the formation of ZnNa_{13} . Subsequently, the diffraction peak of Na_2Se gradually weakens during the charging, until it completely disappears. This process is accompanied by the appearance of Na_xMoSe_2 . Simultaneously, the peak of MoSe_2 starts reappearing and its intensity grows until the end of charging, indicating its full recovery with excellent reversibility. Moreover, the close proximity of some sample

diffraction peaks to those of the substrate made it challenging to observe the variation in the ZnSe diffraction peaks.

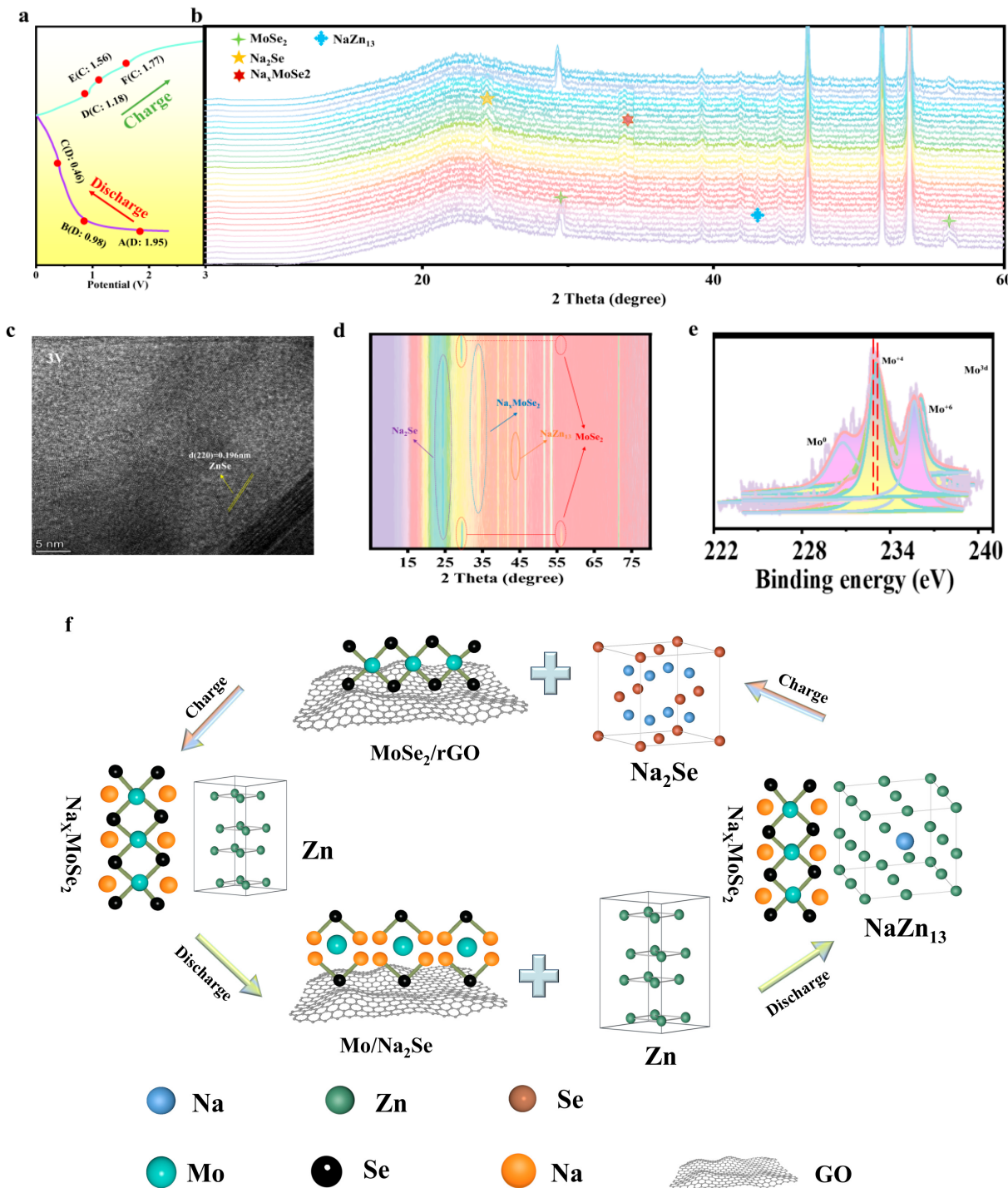


Figure 5. (a,b) In situ stacked XRD patterns of the ZnSe_xMoSe₂/rGO electrode during the initial discharge/charge from a potential of 0.01 to 3.0 V; (c) HRTEM image of the electrode when discharged to 0.01 V; (d) ZnSe_xMoSe₂/rGO electrode; (e) ex situ XPS spectrum of Mo 3d; and (f) schematic diagram illustrating the electrochemical reaction of the ZnSe_xMoSe₂/rGO electrode.

HRTEM is another important technique for identifying intermediate products. Notably, when the electrode was charged to 3 V, a lattice spacing of 0.196 nm was observed on the (220) plane of ZnSe (Figure 5c). Finally, Figure 5d provides an overview of the

ZnSe_xMoSe₂/rGO electrode depicted in Figure 5a,b. Figure 5e shows the ex situ XPS of Mo 3d measured at various stages of charging/discharging. It is evident that, during the discharging process, MoSe₂ is converted into Na_xMoSe₂, and the signal of Mo⁴⁺ gradually shifts in the negative direction. Subsequently, the XPS characteristic peaks reappear during the charging process, indicating the regeneration of MoSe₂ [36]. After full charging, the electrode mainly consists of MoSe₂ and ZnSe, as summarized in Figure 5f, while the rGO substrate remains unchanged. The above in situ XRD, ex situ HRTEM and ex situ XPS strongly support that the ZnSe_xMoSe₂/rGO electrode has a very good reversibility [37].

The following study explores the application of ZnSe_xMoSe₂/rGO composites in SIB full cells [38]. Figure 6a shows the performance of the ZnSe_xMoSe₂/rGO//Na₃V₂(PO₄)₃ battery in the voltage between 1.0 and 3.0 V at 0.1 A g⁻¹. The initial charge and discharge show a specific capacity of 161.5/140.6 mAh g⁻¹ equivalent to 87.1% of ICE. The cycling stability, measured at 0.5 A g⁻¹, maintains a reversible capacity of 112 mAh g⁻¹ after 220 cycles (Figure 6b). The rate performance of the full cell (Figure 6c) reveals discharge-specific capacities of 216.4, 131.2, 127.1, 118.3, 108.2 and 92.9 mAh g⁻¹ at 0.1, 0.2, 0.5, 1.0, 2.0 and 5.0 A g⁻¹, respectively. Notably, the specific capacity reaches 129.8 mAh g⁻¹ when the current density returns to 0.1 A g⁻¹. The remarkable electrochemical performance of the ZnSe_xMoSe₂/rGO//Na₃V₂(PO₄)₃ battery indicates its great potential in future SIB applications.

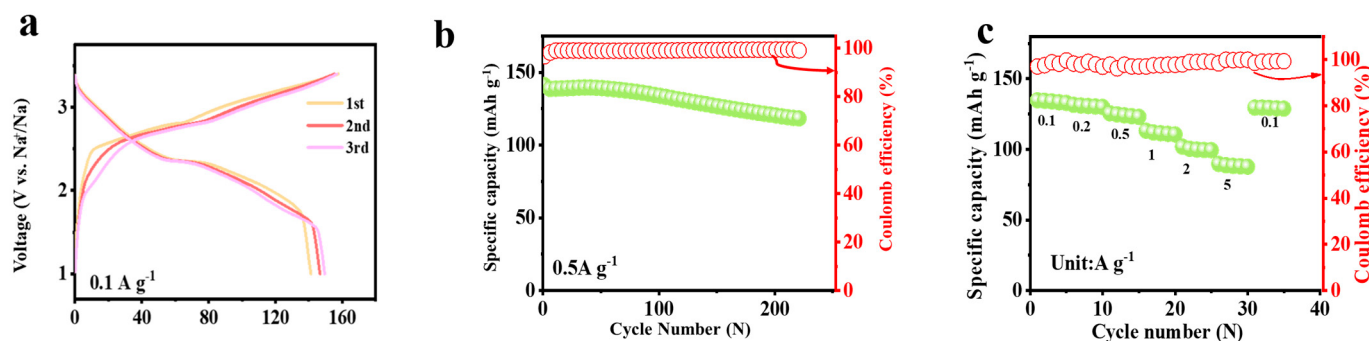


Figure 6. Electrochemical performance of ZnSe_xMoSe₂/rGO//Na₃V₂(PO₄)₃ Na ion full battery: (a) a discharge/charge curve at a current density of 0.1 A g⁻¹; (b) cycling at 0.5 A g⁻¹; and (c) rate performance.

4. Conclusions

This study developed a synthetic method to fabricate porous multi-component hybrids, in which the obtained MoSe₂ flakes are intercalated and decorated by ZnSe nanoparticles and are anchored onto graphene substrates [39]. Using graphene oxides as the starting reagent prevents graphene agglomeration and restrains the size of the MoSe₂ flakes, efficiently resulting in a microstructure that can buffer the volume fluctuation during the charging/discharging. The enlarged interlayer spacing of MoSe₂ also promotes Na⁺ ion diffusion. Integrated with the exceptional mechanical and electrochemical properties of the reduced graphene oxides, the composites exhibit remarkable sodium ion storage performance. Comprehensive in situ and ex situ characterizations shed light on the highly reversible nature of the ZnSe_xMoSe₂/rGO electrode during sodium insertion/extraction. Notably, the composites demonstrate exceptional sodium storage capabilities, where a reversible capacity of 265 mAh g⁻¹ at 20 A g⁻¹ was achieved after 6400 cycles. It could achieve a 235 mAh g⁻¹ capacity even at an ultra-high rate of 30.0 A g⁻¹.

Moreover, a full battery employing Na₃V₂(PO₄)₃ as the cathode and the ZnSe_xMoSe₂/rGO composite as the anode demonstrated an outstanding performance. This strong performance is ascribed to the fact that the rGO substrate enhances the active surface area for ether electrolyte penetration and the presence of ZnSe nanoparticles hinders MoSe₂ nanosheet aggregation [40]. This study presents a synthetic approach and structural design for developing high-performance SIBs and for exploring advanced materials in energy and environmental applications.

Supplementary Materials: The following supporting information can be downloaded at: <https://www.mdpi.com/article/10.3390/batteries10120447/s1>, Figure S1: Schematic representation of the preparation of ZnSe_xMoSe₂/rGO hybrids; Figure S2: (a,b) Morphology and structure of ZnSe_xMoSe₂ hybrids; Figure S3: ZnSe_xMoSe₂ N₂ adsorption isotherms and corresponding pore size distributions; Figure S4: (a) XPS full spectrum of ZnSe_xMoSe₂/rGO; (b) GCD curve of ZnSe_xMoSe₂; Figure S5: (a) CV curves of ZnSe_xMoSe₂ at different scan rates. (b) b-value analysis based on the relationship between peak current and scan rate. (c) Capacitance contribution of ZnSe_xMoSe₂ at a scan rate of 1.0 mV⁻¹ (coloured filled region). (d) Contribution ratio of the capacitive contribution at different scan rates. (e,f) Plot of the variation of the diffusion coefficient of Na⁺; Figure S6: (a,b) The in situ XRD signal formed by ZnNa₁₃; Figure S7: (a) Morphology and structure of MoO₃. (b) XRD of MoO₃; Figure S8: The ICP test of ZnSe_xMoSe₂/rGO.

Author Contributions: H.X. wrote the original draft. S.C. and L.Y. reviewed and edited. G.C., H.J., J.L., S.W. and J.W. supervised and provided funding acquisition. All authors have read and agreed to the published version of the manuscript.

Funding: We are grateful for financial support from the National Natural Science Foundation of China (52272088), the Natural Sciences and Engineering Research Council of Canada (NSERC, DG 03891).

Data Availability Statement: The original contributions presented in this study are included in the article and Supplementary Materials. Further inquiries can be directed to corresponding authors.

Conflicts of Interest: The authors declare no conflicts of interest.

References

- Wang, G.; Lu, Z.; Li, Y.; Li, L.; Ji, H.; Feteira, A.; Zhou, D.; Wang, D.; Zhang, S.; Reaney, I.M. Electroceramics for High-Energy Density Capacitors: Current Status and Future Perspectives. *Chem. Rev.* **2021**, *121*, 6124–6172. [[CrossRef](#)]
- Wu, H.; Xia, G.; Yu, X. Recent progress on nanostructured iron-based anodes beyond metal-organic frameworks for sodium-ion batteries. *EnergyChem* **2023**, *5*, 100095. [[CrossRef](#)]
- Rehman, J.; Lin, S.; Butt, M.K.; Fan, X.; Khattab, T.; Elsayed, K.A.; Shibli, M.F. An overview of 2D metal sulfides and carbides as Na host materials for Na-ion batteries. *Chem. Eng. J.* **2023**, *461*, 141924. [[CrossRef](#)]
- Sun, Y.-K. Direction for Commercialization of O₃-Type Layered Cathodes for Sodium-Ion Batteries. *ACS Energy Lett.* **2020**, *5*, 1278–1280. [[CrossRef](#)]
- Lee, J.; Kim, C.; Choi, K.; Seo, J.; Choi, Y.; Choi, W.; Kim, Y.-M.; Jeong, H.Y.; Lee, J.H.; Kim, G.; et al. In-situ coalesced vacancies on MoSe₂ mimicking noble metal: Unprecedented Tafel reaction in hydrogen evolution. *Nano Energy* **2019**, *63*, 103846. [[CrossRef](#)]
- Zhao, X.; Zhao, Y.; Huang, B.; Yang, Z.; Cai, W.; Sui, J.; Cao, G.; Wang, H.-E. Dual interface coupled molybdenum diselenide for high-performance sodium ion batteries and capacitors. *J. Power Sources* **2020**, *446*, 227298. [[CrossRef](#)]
- Obaidulla, S.M.; Supina, A.; Kamal, S.; Khan, Y.; Kralj, M. van der Waals 2D transition metal dichalcogenide/organic hybridized heterostructures: Recent breakthroughs and emerging prospects of the device. *Nanoscale Horiz.* **2023**, *9*, 44–92. [[CrossRef](#)] [[PubMed](#)]
- Zhang, H.; Tong, C.J.; Zhang, Y.; Zhang, Y.N.; Liu, L.M. Porous BN for hydrogen generation and storage. *J. Mater. Chem. A Mater. Energy Sustain.* **2015**, *3*, 9632–9637. [[CrossRef](#)]
- Guo, J.; Yang, J.; Guan, J.; Chen, X.; Zhu, Y.; Fu, H.; Liu, Q.; Wei, B.; Geng, H. Interface and electronic structure dual-engineering on MoSe₂ with multi-ion/electron transportation channels for boosted sodium-ion half/full batteries. *Chem. Eng. J.* **2022**, *450*, 138007. [[CrossRef](#)]
- Xu, X.; Mai, B.; Liu, Z.; Ji, S.; Hu, R.; Ouyang, L.; Liu, J.; Zhu, M. Self-sacrificial template-directed ZnSe@C as high performance anode for potassium-ion batteries. *Chem. Eng. J.* **2020**, *387*, 124061. [[CrossRef](#)]
- Lin, Z.; Zhang, W.; Peng, J.; Li, Q.; Liang, Z.; Wang, G.; Wang, J.; Wang, G.; Huang, Z.; Huang, S. Synergistic Regulation of Polyselenide Dissolution and Na-Ion Diffusion of Se-Vacancy-Rich Bismuth Selenide toward Ultrafast and Durable Sodium-Ion Batteries. *Adv. Energy Mater.* **2024**, *14*, 2402110. [[CrossRef](#)]
- Gao, L.; Cao, M.; Zhang, C.; Li, J.; Zhu, X.; Guo, X.; Toktarbay, Z. Zinc selenide/cobalt selenide in nitrogen-doped carbon frameworks as anode materials for high-performance sodium-ion hybrid capacitors. *Adv. Compos. Hybrid Mater.* **2024**, *7*, 144. [[CrossRef](#)]
- Alvin, S.; Yoon, D.; Chandra, C.; Cahyadi, H.S.; Park, J.-H.; Chang, W.; Chung, K.Y.; Kim, J. Revealing sodium ion storage mechanism in hard carbon. *Carbon* **2019**, *145*, 67–81. [[CrossRef](#)]
- Hua, R.; Li, H.; Zheng, J.; Wang, R.; Ma, Q.; Zhou, T.; Zhang, L.; Kang, H.; Zhang, C.; Zheng, Y. Spatially confined construction of heterostructured SnSe/SnTe nanodots in porous carbon fibers with high-level N-doping for superior sodium storage. *J. Power Sources* **2023**, *554*, 232333. [[CrossRef](#)]
- Tiwari, V.K.; Singh, R.K. Nanostructured coating strategies of cathode for improved sodium ion battery performance. *Chem. Eng. J.* **2023**, *471*, 144592. [[CrossRef](#)]

16. Tian, H.; Sun, Z.; Ren, L.; Jin, Y.; Wang, D.; Wei, Y.; Chen, H.; Liu, K.; Chen, Y.; Yang, H. Hollow CoSe₂-ZnSe microspheres inserted in reduced graphene oxide serving as advanced anodes for sodium ion batteries. *J. Colloid Interface Sci.* **2024**, *658*, 827–835. [CrossRef]
17. He, Y.; Wang, L.; Dong, C.; Li, C.; Ding, X.; Qian, Y.; Xu, L. In-situ rooting ZnSe/N-doped hollow carbon architectures as high-rate and long-life anode materials for half/full sodium-ion and potassium-ion batteries. *Energy Storage Mater.* **2019**, *23*, 35–45. [CrossRef]
18. Huang, Y.; Wang, Z.; Guan, M.; Wu, F.; Chen, R. Toward Rapid-Charging Sodium-Ion Batteries using Hybrid-Phase Molybdenum Sulfide Selenide-Based Anodes. *Adv. Mater.* **2020**, *32*, 2003534. [CrossRef] [PubMed]
19. Sun, D.; Ye, D.; Liu, P.; Tang, Y.; Guo, J.; Wang, L.; Wang, H. MoS₂/Graphene Nanosheets from Commercial Bulky MoS₂ and Graphite as Anode Materials for High Rate Sodium-Ion Batteries. *Adv. Energy Mater.* **2017**, *8*, 1702383.
20. Ali, Z.; Asif, M.; Huang, X.; Tang, T.; Hou, Y. Hierarchically Porous Fe₂CoSe₄ Binary-Metal Selenide for Extraordinary Rate Performance and Durable Anode of Sodium-Ion Batteries. *Adv. Mater.* **2018**, *30*, 1802745. [CrossRef] [PubMed]
21. Zhao, Y.; Wei, C.; Sun, S.; Wang, L.P.; Xu, Z.J. Reserving Interior Void Space for Volume Change Accommodation: An Example of Cable-Like MWNTs@SnO₍₂₎@C Composite for Superior Lithium and Sodium Storage. *Adv. Sci.* **2015**, *2*, 1500097. [CrossRef] [PubMed]
22. Zhao, K.; Liu, F.; Niu, C.; Xu, W.; Dong, Y.; Zhang, L.; Xie, S.; Yan, M.; Wei, Q.; Zhao, D.; et al. Graphene Oxide Wrapped Amorphous Copper Vanadium Oxide with Enhanced Capacitive Behavior for High-Rate and Long-Life Lithium-Ion Battery Anodes. *Adv. Sci.* **2015**, *2*, 1500154. [CrossRef] [PubMed]
23. Zhang, Y.; Cheng, L.; Li, L.; Lin, Y.; Li, S.; Li, Y.; Ren, X.; Zhang, P.; Sun, L. ZnSe/SnSe Heterostructure Incorporated with Selenium/Nitrogen Co-Doped Carbon Nanofiber Skeleton for Sodium-Ion Batteries. *Small* **2024**, *20*, e2306536. [CrossRef] [PubMed]
24. Dong, C.; Wu, L.; He, Y.; Zhou, Y.; Sun, X.; Du, W.; Sun, X.; Xu, L.; Jiang, F. Willow-Leaf-Like ZnSe@N-Doped Carbon Nanoarchitecture as a Stable and High-Performance Anode Material for Sodium-Ion and Potassium-Ion Batteries. *Small* **2020**, *16*, e2004580. [CrossRef] [PubMed]
25. Pan, X.; Xi, B.; Lu, H.; Zhang, Z.; An, X.; Liu, J.; Feng, J.; Xiong, S. Molybdenum Oxynitride Atomic Nanoclusters Bonded in Nanosheets of N-Doped Carbon Hierarchical Microspheres for Efficient Sodium Storage. *Nanomicro Lett.* **2022**, *14*, 163. [CrossRef]
26. Mao, J.; Yu, Y.; Wang, L.; Zhang, X.; Wang, Y.; Shao, Z.; Jie, J. Ultrafast, Broadband Photodetector Based on MoSe(2)/Silicon Heterojunction with Vertically Standing Layered Structure Using Graphene as Transparent Electrode. *Adv. Sci.* **2016**, *3*, 1600018. [CrossRef] [PubMed]
27. Xin, G.; Yao, T.; Sun, H.; Scott, S.M.; Shao, D.; Wang, G.; Lian, J. Highly thermally conductive and mechanically strong graphene fibers. *Science* **2015**, *349*, 1083–1087. [CrossRef]
28. Qiu, X.-P.; Liu, X.; Jiang, S.-M.; Jiang, G.-R.; Zhang, Q.-F. Growth mechanism for zinc coatings deposited by vacuum thermal evaporation. *J. Iron Steel Res. Int.* **2021**, *28*, 1047–1053. [CrossRef]
29. Guo, Z.; Ye, Z.; Yin, M.; Dai, S.; Zhang, X.; Wang, W.; Liu, Z. Growth of Low-Defect Nitrogen-Doped Graphene Film Using Condensation-Assisted Chemical Vapor Deposition Method. *Materials* **2023**, *16*, 1120. [CrossRef] [PubMed]
30. An, N.; Li, W.; Shao, Z.; Zhou, L.; He, Y.; Sun, D.; Dong, X.; Hu, Z. Graphene oxide coated polyaminoanthraquinone@MXene based flexible film electrode for high-performance supercapacitor. *J. Energy Storage* **2023**, *57*, 106180. [CrossRef]
31. Yao, Z.; Yu, C.; Dai, H.; Zhou, J.; Liu, X.; Sun, G. Hybrid fibers assembled from MoSe₂/graphene heterostructures endow improved supercapacitive performance. *Carbon* **2022**, *187*, 165–172. [CrossRef]
32. Lee, J.; Kwon, S.; Kim, T.; Jung, J.; Zhao, L.; Lee, J.H. Nonlinear optical property measurements of rhenium diselenide used for ultrafast fiber laser mode-locking at 1.9 μm. *Sci. Rep.* **2021**, *11*, 9320.
33. Zhou, Y.; Zhang, M.; Han, Q.; Liu, Y.; Wang, Y.; Sun, X.; Zhang, X.; Dong, C.; Jiang, F. Hierarchical 1 T-MoS₂/MoO_x@NC microspheres as advanced anode materials for potassium/sodium-ion batteries. *Chem. Eng. J.* **2022**, *428*, 131113. [CrossRef]
34. He, Z.; Yao, L.; Guo, W.; Sun, N.; Wang, F.; Wang, Y.; Wang, R.; Wang, F. Pseudocapacitance of Bimetallic Solid-Solution MXene for Supercapacitors with Enhanced Electrochemical Energy Storage. *Adv. Funct. Mater.* **2023**, *33*, 2305251. [CrossRef]
35. Zhang, Y.; Huang, Y.; Srot, V.; van Aken, P.A.; Maier, J.; Yu, Y. Enhanced Pseudo-Capacitive Contributions to High-Performance Sodium Storage in TiO₍₂₎/C Nanofibers via Double Effects of Sulfur Modification. *Nanomicro Lett.* **2020**, *12*, 165.
36. Hu, X.; Zhu, R.; Wang, B.; Liu, X.; Wang, H. Dual Regulation of Metal Doping and Adjusting Cut-Off Voltage for MoSe(2) to Achieve Reversible Sodium Storage. *Small* **2022**, *18*, e2200437. [CrossRef] [PubMed]
37. Li, Z.; Yu, L.; Tao, X.; Li, Y.; Zhang, L.; He, X.; Chen, Y.; Xiong, S.; Hu, W.; Li, J.; et al. Honeycomb-Structured MoSe₂/rGO Composites as High-Performance Anode Materials for Sodium-Ion Batteries. *Small* **2023**, *20*, e2304124. [CrossRef] [PubMed]
38. Wang, Q.; Zhang, R.; Sun, D.; Wang, H.; Tang, Y. Manipulating Electrolyte Interface Chemistry Enables High-Performance TiO Anode for Sodium-Ion Batteries. *Batteries* **2024**, *10*, 362. [CrossRef]
39. Jo, D.Y.; Park, S.K. Facile Fabrication of Porous MoSe/Carbon Microspheres via the Aerosol Process as Anode Materials in Potassium-Ion Batteries. *Batteries* **2024**, *10*, 25. [CrossRef]
40. Jiang, M.; Abdullah, M.; Chen, X.; E, Y.; Tan, L.; Yan, W.; Liu, Y.; Jiang, W. Two-Step Synthesis of ZnS-NiS Composite with Rough Nanosphere Morphology for High-Performance Asymmetric Supercapacitors. *Batteries* **2024**, *10*, 16.

Disclaimer/Publisher's Note: The statements, opinions and data contained in all publications are solely those of the individual author(s) and contributor(s) and not of MDPI and/or the editor(s). MDPI and/or the editor(s) disclaim responsibility for any injury to people or property resulting from any ideas, methods, instructions or products referred to in the content.